JOURNAL OF PETROLOGY | VOLUME 53 | NUMBER 3 | PAGES 589–609 | 2012 | doi:10.1093/petrology/egr072

Crystallization Stages of the Bishop Tuff Magma Body Recorded in Crystal Textures in Pumice Clasts

AYLA S. PAMUKCU[1]*, GUILHERME A. R. GUALDA[1] AND ALFRED T. ANDERSON, JR[2]

[1]DEPARTMENT OF EARTH AND ENVIRONMENTAL SCIENCES, VANDERBILT UNIVERSITY, NASHVILLE, TN 37240, USA
[2]DEPARTMENT OF GEOPHYSICAL SCIENCES, UNIVERSITY OF CHICAGO, CHICAGO, IL 60637, USA

RECEIVED JANUARY 7, 2011; ACCEPTED NOVEMBER 23, 2011
ADVANCE ACCESS PUBLICATION JANUARY 23, 2012

The Bishop Tuff is a giant silicic ignimbrite erupted at 0·76 Ma in eastern California, USA. Five pumice clasts from the late-erupted Bishop Tuff (Aeolian Buttes) were studied in an effort to better understand the pre- and syn-eruptive history of the Bishop magma body and place constraints on the timescales of its existence. This study complements and expands on a previous study that focused on early-erupted Bishop Tuff pumice clasts. Bulk densities of pumice clasts were measured using an immersion method, and phenocryst crystal contents were determined using a sieving and winnowing procedure. X-ray tomography was used to obtain qualitative and quantitative textural information, particularly crystal size distributions (CSDs). We have determined CSDs for crystals ranging in size from ~10 to ~1000 μm for three groups of mineral phases: magnetite (±ilmenite), pyroxene + biotite, quartz + feldspar. Similar to early-erupted pumice, late-erupted pumice bulk density and crystal contents are positively correlated, and comparison of crystal fraction vs size trends suggests that the proportion of large crystals is the primary control on crystallinity. Porosity is negatively correlated with crystal content, which is difficult to reconcile with closed-system crystallization. Magnetite and pyroxene + biotite size distributions are fractal in nature, often attributed to fragmentation; however, crystals are mostly whole and euhedral, such that an alternative mechanism is necessary to explain these distributions. Quartz + feldspar size distributions are kinked, with a shallow-sloped log–linear section describing large crystals (>140 μm) and a steep-sloped log–linear section describing small crystals (<140 μm). We interpret these two crystal populations as resulting from a shift in crystallization regime. We suggest that the shallow-sloped section describes a pre-eruptive quartz + feldspar growth-dominated regime, whereas the steep-sloped section represents a population that grew during a nucleation-dominated regime that began as a result of decompression at the onset of eruption. Timescales of quartz growth calculated from the slopes of these two segments of the size distributions indicate that the pre-eruptive crystal population grew on timescales on the order of millennia and may describe the timescale of crystallization of the Bishop magma body. The syn-eruptive population gives timescales of <1–2 years (but possibly much less) and probably marks the onset of eruptive decompression.

KEY WORDS: *Bishop Tuff; crystal size distributions; textures; supereruptions; X-ray tomography*

BACKGROUND AND MOTIVATION

The existence of giant magma reservoirs within the Earth's crust is evidenced most strikingly by huge pyroclastic deposits, often comprising hundreds to thousands of km^3 (Self, 2006), inferred to have erupted in a matter of days to weeks (Smith & Bailey, 1966; Ledbetter & Sparks, 1979; Wilson & Hildreth, 1997). The size of the deposits and the potential threat that similar eruptions pose to society (Lowenstern *et al.*, 2006) make these deposits both interesting and important to study. In trying to understand the history and evolution of these large magma bodies, we gain significant insights into igneous systems in general, as well as information that may become useful in efforts to predict future supereruptions.

The Bishop Tuff (Fig. 1) is a very well-studied example of a giant silicic eruption. The Bishop Tuff stratigraphy and

*Corresponding author. Telephone: 615-322-2976.
E-mail: ayla.s.pamukcu@vanderbilt.edu

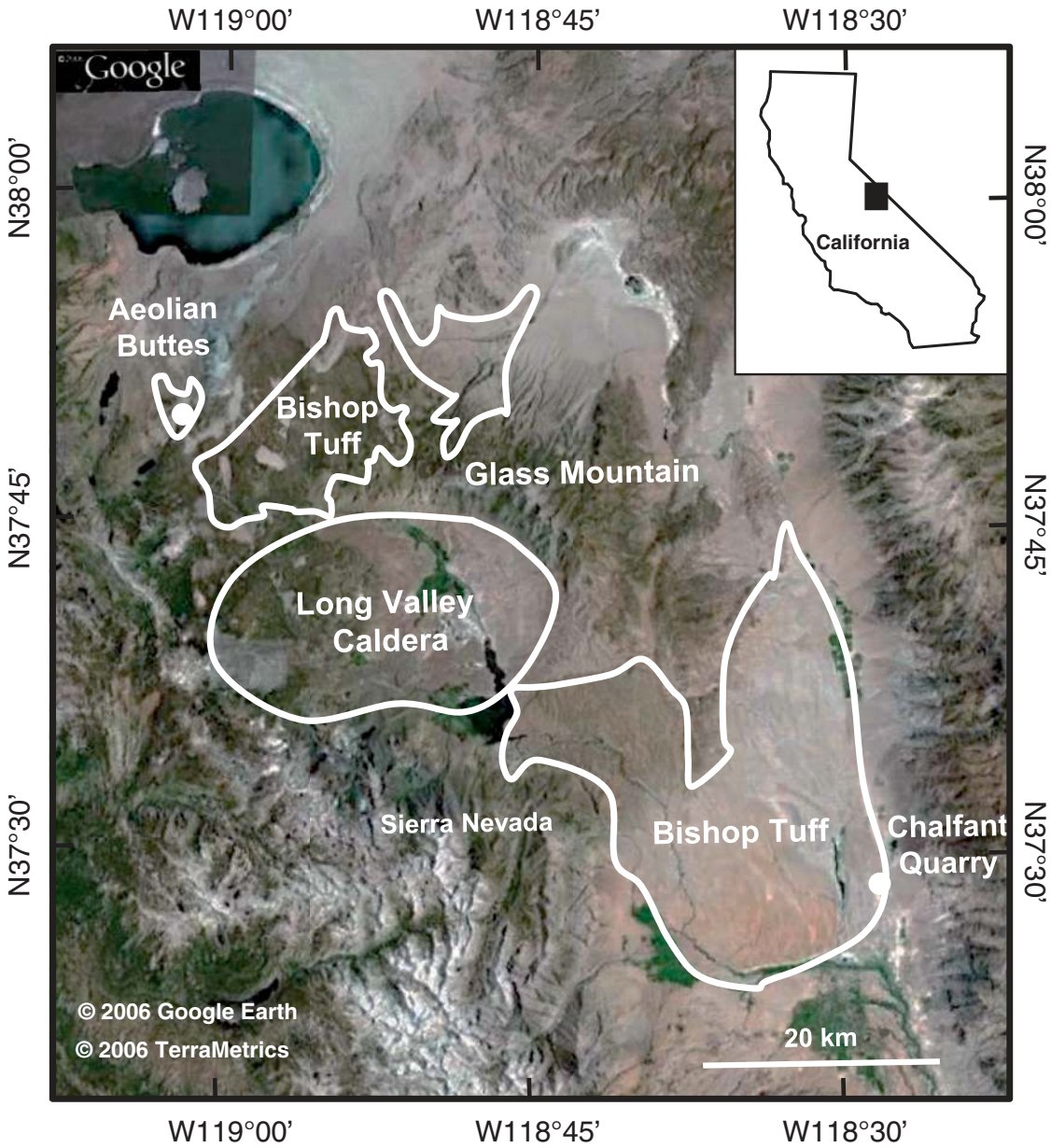

Fig. 1. Map of the Long Valley region in central eastern California showing the distribution of the Bishop Tuff. Map of distribution simplified from Hildreth and Mahood (1986) overlain on Google Earth image. Late-erupted samples were collected from the Aeolian Buttes location. Early-erupted samples are from the Chalfant Quarry.

petrography (Bailey *et al.*, 1976; Hildreth, 1977, 1979; Wilson & Hildreth, 1997), whole-rock geochemistry (Hildreth, 1977; Wilson & Hildreth, 1997), geochronology (for a review, see Simon & Reid, 2005), and mineral and melt inclusion compositions (e.g. Hildreth, 1977, 1979; Wallace *et al.*, 1999; Anderson *et al.*, 2000; Hervig & Dunbar, 1992; among many others) have been studied in some detail.

Compositional zonation of the Bishop magma body has been inferred based on a number of lines of evidence, particularly the stratigraphic zonation of the deposit as a whole (Hildreth, 1977; Hildreth & Wilson, 2007), major, trace and O isotope compositions of phenocrysts (Hildreth, 1979; Bindeman & Valley, 2002), and volatile and trace-element compositions of melt inclusions (Hervig & Dunbar, 1992; Wallace *et al.*, 1995, 1999; Anderson *et al.*, 2000). This compositional stratigraphy of the Bishop Tuff mainly reflects variation that developed prior to the onset of the eruption, as indicated by the pressures of formation ($\geq$1000 atm) of melt inclusions in phenocrysts. U–Pb zircon ages span an interval of >100 kyr prior to

eruption (Simon & Reid, 2005), and have been inferred to represent the timescales of existence of the Bishop magma body. Stratigraphic relations (Wilson & Hildreth, 1997) suggest that eruption of the Bishop Tuff was short-lived, giving a temporal framework of some 125 h of continuing eruption, with only one or two short breaks.

It is natural to expect that such dramatic changes in the prevailing conditions would be reflected in crystal and bubble populations, and textures may provide a particularly useful record of the different stages in the evolution of the Bishop magma. Thus, in this work we focus on crystal textures as a means to better understand the history of the Bishop magma and, more generally, to better understand magmatic evolution in a giant magma reservoir.

Crystal size distributions are a useful tool in textural studies of igneous rocks, as they can reveal information about crystal nucleation and growth histories in magmas (e.g. Cashman & Marsh, 1988; Marsh, 1988*b*, 1998, 2007; Bindeman, 2003). Additionally, they have been used to suggest multiple stages of magmatic crystallization (e.g. Cashman, 1988) and to estimate the timescales of magmatic crystallization (Cashman, 1988, 1992, 1993; Cashman & Marsh, 1988). Fragment size distributions have been used to document crystal fragmentation and characterize fragmentation mechanisms (Bindeman, 2005; Gualda, 2006). These prior studies provide a framework to interpret quantitative textural information as it pertains to the pre- and syn-eruptive crystallization of the Bishop magma.

SAMPLE DESCRIPTION

The pumice clasts focused on in this study are from the ash flow exposed on the hill known as Aeolian Buttes and designated as Bishop Tuff stratigraphic unit Ig2NWb by Wilson & Hildreth (1997). The Aeolian Buttes hill is in section 14 of T 1S and R 26 E (UTM metric grid 17.4 east/92.1 north, approximately), about 12 km north of the caldera rim and the California highway maintenance station at Crestview on US Highway 395. The Bishop Tuff is lightly welded in the upper parts of the Aeolian Buttes (above about 2230 m) and densely welded with black glassy fiamme at elevations below about 2170 m.

The lightly welded Ig2NWb Bishop Tuff forms blocks and towers up to ~7 m high that lie on boulders and blocks of granite (Cretaceous). Commonly, the tuff is eroded away at the contact forming a notch 10–50 cm in vertical extent; it is possible that even more tuff has been removed during erosion and that the overlying block of lightly welded tuff has subsided as unwelded tuff at the contact was eroded away. The amount of subsidence is important as it telescopes the lowermost, most rapidly cooled tuff yielding an apparently steeper fossil temperature gradient into the overlying, more slowly cooled tuff. The high degree of welding and abundant glassy fiamme suggest that the Ig2NWb ash flow was qualitatively hot enough to cause dense welding, but it cooled rapidly so that fiamme remained glassy. Importantly for this study, the lightly welded tuff is uncompacted such that the porosity and vesicles in the pumice have preserved their original properties from their time of deposition. The original tuff was evidently thinner over a hill of granite and thicker above the highly welded tuff at lower elevations.

The Ig2NWb Bishop Tuff at Aeolian Buttes contains many unwelded to slightly welded pumice blocks up to about 30 cm diameter. Most of these have buff to reddish brown rims up to about 4 cm thick and white cores (Fig. 2), reflecting a range of oxidation and cooling histories and permeabilities.

Hildreth & Wilson (2007) classified Bishop pumice clasts into seven common and seven rare types based on texture and crystal content. Four of our Ig2NWb clasts (AB.530l, AB.6202, AB.6203 and AB.xx02) contain more than 20 wt. % of phenocrysts (Table 1, Fig. 2) and fall into their crystal-rich Adobe sub-type, which is dominant in Ig2NWb. However, clast AB.xx02 contains an exceptionally large number of vesicles larger than about 5 mm diameter. Our other Ig2NWb clast (AB.620l; see Fig. 2) has a modest crystal content and is relatively low in bulk density and rich in small vesicles, corresponding roughly to sub-type 'swirly'. Hildreth & Wilson (2007) noted that their swirly sub-type contains the 'Lowest density clasts in the Bishop', although they did not report quantitative clast densities.

METHODS

Five properties of each late-erupted pumice clast were analyzed: clast mass, bulk density, crystallinity, porosity, and crystal size distribution (CSD). Bulk density determinations were accomplished using an immersion method developed and applied in previous studies (e.g. Skirius *et al.*, 1990). A physical separation process based on crushing, sieving and winnowing was used to determine crystal and glass mass fractions, as well as bulk porosities. Finally, X-ray tomography was used to measure crystal size distributions.

Bulk density determination

The method used for bulk density determinations—based on Archimedes' principle—has been used in previous studies on the Bishop Tuff pumice (e.g. Gualda *et al.*, 2004) and has been described in detail by Gualda (2007). Each pumice clast was first lightly cleaned with a dry brush to reduce the presence of extraneous dust and material. This 'dry' clast was then weighed. Next, the clast was covered with a thin layer of Silly Putty (just enough to seal the sample completely), which was subsequently molded closely to the clast's form, and extraneous putty was discarded. The Silly Putty-covered clast was then weighed while submerged in a tub of water to determine the

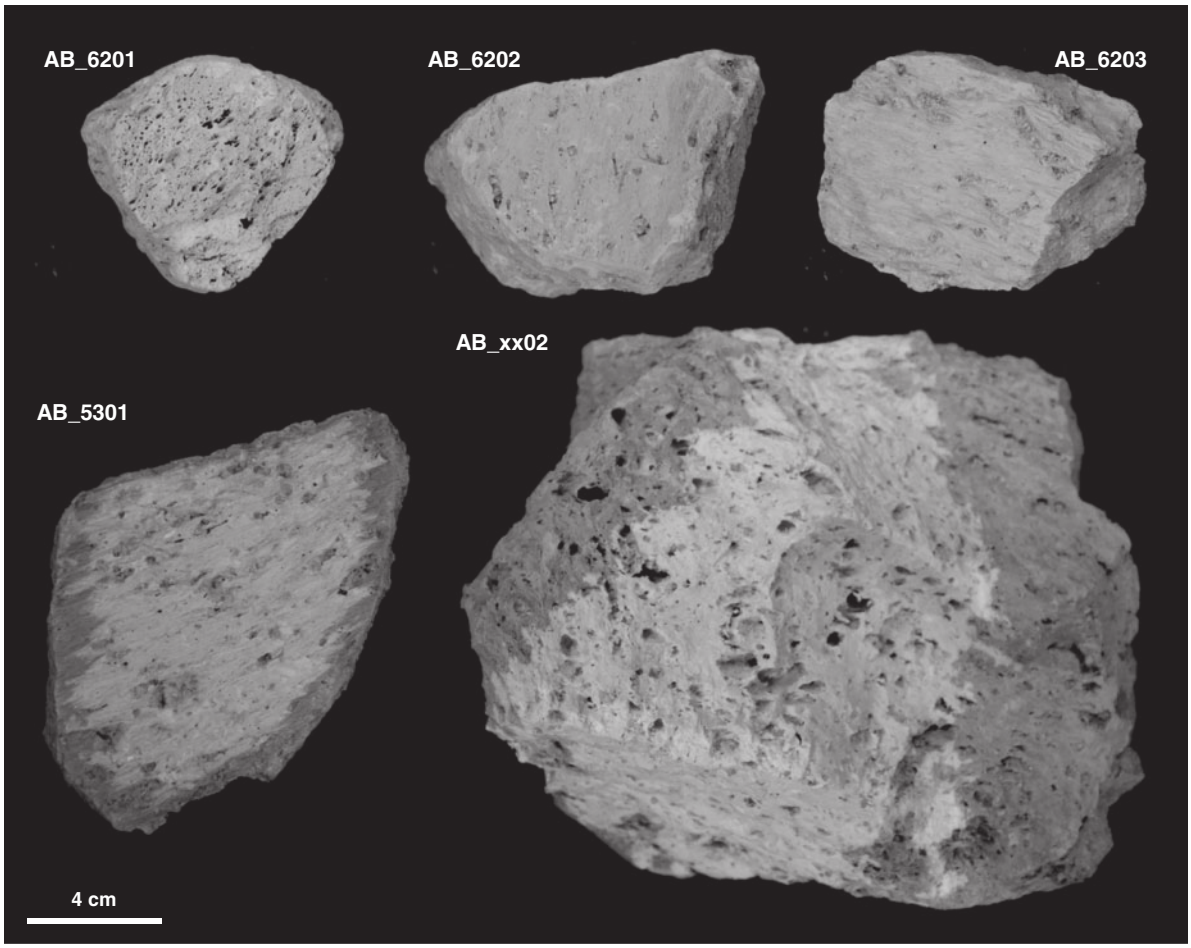

Fig. 2. Pumice clasts from the late-erupted Bishop Tuff (Aeolian Buttes). The lowest-density clast (AB.6201) has few crystals and many small vesicles. Two of the intermediate-density clasts (AB.6202, AB.6203) are very similar to each other, with large crystals and low porosity. The third intermediate-density clast (AB.xx02) is notably different, with large and abundant vesicles. The high-density clast (AB.5301) is significantly more crystal-rich than the other samples. A noteworthy feature is the white cores and darker (orange) rinds of pumice clasts AB.5301 and AB.xx02, revealing potentially different cooling histories for the rind and core regions; pieces studied from these pumice clasts were cut from the white regions.

weight of the 'wet' clast (often yielding negative weight). The putty was then removed and weighed separately. A bulk density measurement for each pumice clast was obtained using the measured weights and the formula of Gualda *et al.* (2004).

Crystal separation

Crystal concentrates were separated from the bulk pumice using the crushing, sieving and winnowing technique employed by Gualda *et al.* (2004) on early-erupted samples. The goal of this process was to determine pumice clast bulk crystallinity (crystal mass fraction), from which bulk porosity (pore volume fraction) can be calculated if the bulk density is known. Crystal size distribution information can be derived using this procedure, but is variably affected by laboratory fragmentation.

Physical separation consisted of sample crushing followed by a series of sieving and winnowing steps. A small piece from each pumice clast (8·5–13 g) was crushed. Effort was made to avoid artificial crystal fragmentation by crushing as lightly and as little as possible. Crushed material was subsequently separated through a series of five sieves: 1·8, 0·8, 0·5, 0·2 and 0·1 mm. Each size fraction of sieved material was then winnowed to separate crystals from ash. Separates were dried in an oven and weighed, which yields mass fractions of both crystal and ash separates. In combination with single clast bulk densities, bulk porosity can be computed; an average crystal density of $2{\cdot}65\,\mathrm{g\,cm^{-3}}$ and a glass density of $2{\cdot}30\,\mathrm{g\,cm^{-3}}$ were used (for details, see Gualda *et al.*, 2004; Gualda, 2007).

X-ray tomography

X-ray tomography is an ideal tool for studying the textures of pumice clasts (see Gualda & Rivers, 2006; Gualda *et al.*, 2010; Pamukcu & Gualda, 2010), as it provides three-dimensional (3D) images (i.e. tomograms) of pumice

Table 1: Bulk densities, crystallinities (crystal mass fraction), and porosities (pore volume fraction) for early- and late-erupted pumice clasts (see Fig. 5)

Sample	Location sampled	Unit	Bulk density ($g\,cm^{-3}$)	Crystal fraction (wt. %)	Porosity (vol. %)
F7-14*	Chalfant Quarry	F7	0·63	9·30	72·81
F7-12*	Chalfant Quarry	F7	0·50	6·63	78·52
F8-15*	Chalfant Quarry	F8	0·90	14·35	61·62
Ia-13*	Chalfant Quarry	Ig2E	0·62	9·53	73·64
Ia-15*	Chalfant Quarry	Ig2E	0·76	15·25	67·73
IbA1†	Chalfant Quarry	Ig2E	0·81	16·60	65·66
AB__5301	Aeolian Buttes	Ig2NW	1·18	32·20	51·27
AB__6201	Aeolian Buttes	Ig2NW	0·42	6·63	82·02
AB__6202	Aeolian Buttes	Ig2NW	0·78	25·32	67·42
AB__6203	Aeolian Buttes	Ig2NW	0·98	25·90	59·08
AB__xx02	Aeolian Buttes	Ig2NW	0·74	21·85	68·66

*Gualda *et al.* (2004).
†A. T. Anderson (unpublished data).

clasts that can be used to study crystals and vesicles *in situ* and in three dimensions. The physical characteristics of single crystals (e.g. crystal shape, presence of fractures) and relationships between crystals (e.g. clustering, presence of inclusions) can be documented (Fig. 3a), and stereological corrections—an important source of uncertainties in crystal size distribution studies—are entirely avoided. In addition, unlike physical separation techniques, X-ray tomography is relatively non-destructive, which is fortunate given that Gualda & Rivers (2006) and Gualda (2006) showed that fragmentation during laboratory processing is significant.

All tomographic imaging was performed on the bending magnet beamline of the GeoSoilEnvironCARS (GSECARS) sector of the Advanced Photon Source at Argonne National Laboratory. Detailed descriptions and illustration of the experimental setup at GSECARS have been given by Rivers *et al.* (1999) and Gualda & Rivers (2006). Incident beam energies were between 16 and 24 keV, and images of an YYG scintillator were captured using a CCD camera every 0·25°, in a total of 720 frames and a total rotation of 180°.

Tomogram reconstruction from raw data and visualization (e.g. Fig. 3) were carried out using 'tomo_display' (Rivers & Gualda, 2009). Texture quantification was performed using the 3D image processing tools implemented in Blob3D (Ketcham, 2005). Volume renderings—including associated animations (see Discussion, Fig. 1 of Supplementary Data, available for downloading at http://www.petrology.oxfordjournals.org)—were generated from the output of Blob3D using 'vol_tools' (Rivers & Gualda, 2009).

To cover a suitably large spectrum of crystal sizes (i.e. ~10–1000 μm), our approach was to analyze five cylinders of systematically varying volume from each of the five pumice clasts (see Fig. 4). Size distributions were determined for each cylinder and combined, following the method of Pamukcu & Gualda (2010), to obtain an overall crystal size distribution for each pumice clast.

The linear attenuation coefficient reconstructed for each volume element (or voxel) of a tomogram is a function of the voxel density and mean atomic number. We make use of the fact that mineral phases in a sample have very limited ranges of density and mean atomic number to identify the various phases present as a function of the observed linear attenuation coefficients. Because the 3D maps can be visualized in grayscale, it is possible to visually discern single phases in a tomogram (Fig. 3b); in this sense, tomographic slices are similar to back-scattered electron images—phases with a low linear attenuation coefficient (e.g. air) appear dark, those with a high linear attenuation coefficient (e.g. magnetite) appear bright, and those of intermediate composition appear with intermediate brightness. Phases with significantly different linear attenuation coefficients, such as magnetite and air, are easy to separate and quantify using image processing. However, phases with similar density and mean atomic number (e.g. quartz and feldspar) can be difficult or impractical to separate (for details, see Gualda & Rivers, 2006).

Given that work with early-erupted pumice (Gualda, 2004; Gualda & Rivers, 2006) showed that quartz is much more abundant than sanidine and plagioclase, and that crystal size distributions for quartz and sanidine have similar shapes, we chose to simplify the processing and consider quartz and feldspar in combination. Similarly, we did not distinguish between biotite and pyroxene; these are much less abundant and it becomes difficult to reliably distinguish between them when crystals are relatively small (i.e. <100 voxels). We note that mixed CSDs can be problematic for making interpretations if the growth rates of the two phases are considerably different or if the two phases exist in near equal proportions; however, in both of these cases we would expect to see complex CSDs, which we do not (see below).

We thus distinguish three components: magnetite (±ilmenite); pyroxene + biotite; quartz + sanidine (+minor plagioclase). By limiting the number of components being studied, we were able to (1) study a much larger number of tomograms than would be possible otherwise, and (2) determine crystal size distributions over a wider range of crystal sizes (~10–1000 μm), far outweighing the shortcomings of studying mineral phases in combination.

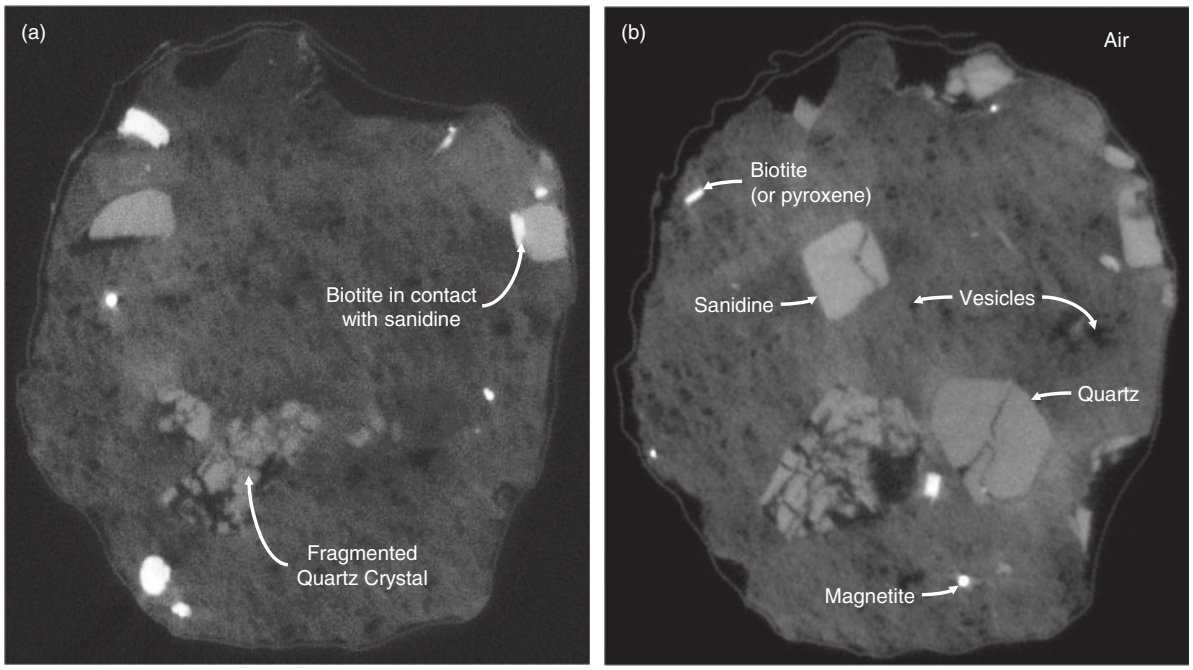

Fig. 3. Tomographic slices through tomograms of late-erupted Bishop pumice clasts. Brightness in the image corresponds to the linear attenuation coefficient, which is proportional to the mean atomic number and density of each volume element (voxel) (for details, see Gualda & Rivers, 2006). Magnetite appears bright, air is dark, and other phases show intermediate brightness. (a) Textural relationships (e.g. crystal fragmentation, clustering, and contact relationships) can be observed in the tomograms and some can be quantified (e.g. size, aspect ratio). (b) Six distinct phases (vesicles + air, glass, quartz, sanidine, pyroxene + biotite, magnetite) can be qualitatively recognized in our samples; however, only five of these phases can be quantitatively assessed (vesicles + air, glass, quartz + feldspar, pyroxene + biotite, magnetite; see text for details). Pixel size is 17 μm; width of the field of view is 11·05 mm.

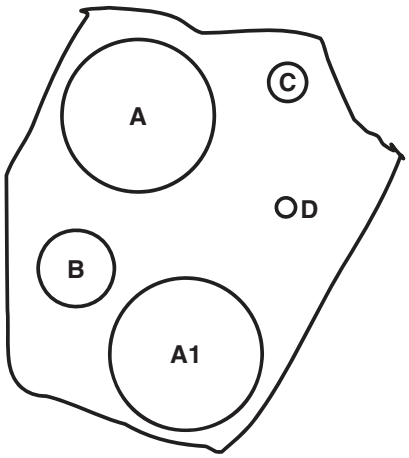

Run	*Resolution (μm/voxel)*	*Sample volume (mm³)*
A, A1	17	700-800
B	8.5	90-115
C	4.5	13-16
D	2.5	1-2.5

Fig. 4. Schematic illustration of sample preparation. Five cylinders of varying size were cut from each pumice clast. The resolution of the tomographic images is determined by the sample size. It should be noted that sample volumes decrease by a factor of ~8 with each ~2-fold increase in resolution. [For more details, see Pamukcu & Gualda (2010).]

RESULTS

Bulk pumice properties

Bulk densities determined for our five late-erupted pumice clasts from Aeolian Buttes show significant variation between clasts, ranging from 0·42 to 1·18 g cm^{-3}. Early-erupted clasts studied by Gualda *et al.* (2004) encompass a similar but smaller range of densities, ranging from 0·5 to 0·9 g cm^{-3} (Table 1); the ranges are similar to those observed by others (e.g. Skirius *et al.*, 1990; Wallace *et al.*, 1999; Anderson *et al.*, 2000; Anderson, 2010). Overall, the densities of late-erupted pumice clasts tend to be higher

than those of early-erupted pumice clasts, the main exception being sample AB.6201, which has a density lower than those measured for early-erupted pumice clasts (Gualda *et al.*, 2004). Although only a small number of pumice clasts have been documented, existing data suggest that higher-density clasts are more common in late-erupted pumice whereas low-density clasts are more common in early-erupted pumice. It is uncertain if the higher average densities in late-erupted pumice reflect different proportions of different kinds of pumice, or whether they reflect higher average densities for the same types of pumice. Sample AB.6201 has a density lower than the densities measured for early-erupted pumice clasts by Gualda *et al.* (2004), but Anderson (2010) has documented some early-erupted clasts with densities as low as $\sim 0{\cdot}26\ \mathrm{g\ cm^{-3}}$.

Crystallinity and porosity values determined for late-erupted pumice clasts indicate a strong positive correlation between crystallinity and bulk density, as well as a strong negative correlation between crystallinity and porosity (Fig. 5), in agreement with results for early-erupted pumice clasts (Gualda *et al.*, 2004).

The crystal contents of our clasts (Table 1) are similar to but greater than those for most clasts of Ig2NWb (Adobe type) reported by Hildreth & Wilson (2007). It is likely that our sample preparation procedure overestimates the amount of crystals. The procedures are such that loss of both crystals and glass occurs during crystal separation. Reported crystal masses include glass adhering to large crystals in the crystal-rich fraction, which probably more than offset mass lost owing to crystals included in pumice pieces in the glass-rich fraction. Our estimated crystal contents may be high by about 2–10% of the amount recorded, depending on the pumice friability, and thickness and completeness of adhering glass. Further work is needed to establish the amounts of crystals in pumice clasts more accurately.

Crushing and sieving data

Our physical separation procedure yields information on the distribution of crystal mass as a function of sieve size (Fig. 6). These data have to be analyzed with caution, given the potential for crystal breakage during crushing. Nonetheless, we notice that all clasts have similar crystal abundances at sizes $<250\ \mu m$, with the exception of clast AB.6202. Crystal mass fraction increases sharply with size (with the exception of the low-density clast AB.6201), showing not only that the large crystals dominate the total crystal mass, but also that the differences in crystal mass and bulk density between the various clasts are explained by the presence and abundance of large (i.e. $>500\ \mu m$) crystals (see Figs 6 and 7a–c). This is very similar to what was determined for the early-erupted pumice (Gualda *et al.*, 2004).

Crystal size distributions

Crystal size distributions for magnetite, pyroxene + biotite, and quartz + feldspar in the late-erupted pumice were obtained using X-ray tomography.

Magnetite and pyroxene + biotite

Magnetite and pyroxene + biotite size distributions for the five late-erupted clasts are similar (for details and figures, see Pamukcu & Gualda, 2010). For both phases, the size distributions for all the samples are concave-up with a paucity of large crystals and enrichment of very small crystals. When plotted on log–log scale, these distributions appear as straight lines indicative of power-law, or fractal, distributions (Marsh, 1998; Bindeman, 2005; Higgins, 2006).

In the case of magnetite, these distributions differ from the magnetite size distributions determined for the early-erupted clasts, which were log–linear and did not show this fractal characteristic (Gualda & Rivers, 2006). However, the crystal size distributions for magnetite in the early-erupted clasts are based on a small number of crystals, and the associated uncertainties are large, such that the possibility that early- and late-erupted magnetite size distributions are actually similar cannot be ruled out.

A similar comparison of early- and late-erupted pyroxene + biotite size distributions is difficult given the very small number of biotite crystals found in the studied early-erupted pumice clasts (see Gualda & Rivers, 2006).

Quartz + feldspar

The size distributions obtained for quartz + feldspar are distinct from those of magnetite and pyroxene + biotite as they do not follow the same smooth concave-up, power-law pattern (Fig. 8a). All five quartz + feldspar distributions are similar in that each distribution follows a general pattern of decreasing population density with increasing size.

The curves can be parsed into three distinct parts (Fig. 8b): (1) a steep curve for small crystal sizes ($\leq 140\ \mu m$); (2) a shallow curve for large crystal sizes ($\geq 140\ \mu m$); (3) a more or less distinct drop in population density between regions (1) and (2). In more detail, quartz + feldspar size distributions are variable from sample to sample (Fig. 9), and the differences correlate with variations in clast bulk density (Fig. 9), as discussed below.

Intermediate-density clasts are the more common class (three samples); thus, for presentation purposes, we describe first the intermediate-density quartz + feldspar size distributions and then discuss how high- and low-density pumice clasts deviate from this pattern.

Intermediate-density clasts. For intermediate-density clasts AB.6202 ($0{\cdot}74\ \mathrm{g\ cm^{-3}}$), AB.6203 ($0{\cdot}78\ \mathrm{g\ cm^{-3}}$) and AB.xx02 ($0{\cdot}98\ \mathrm{g\ cm^{-3}}$), high population densities typical of Part (1) of the size distribution are seen for crystals $<35\ \mu m$; the shallow slopes typical of Part (2) appear for crystals

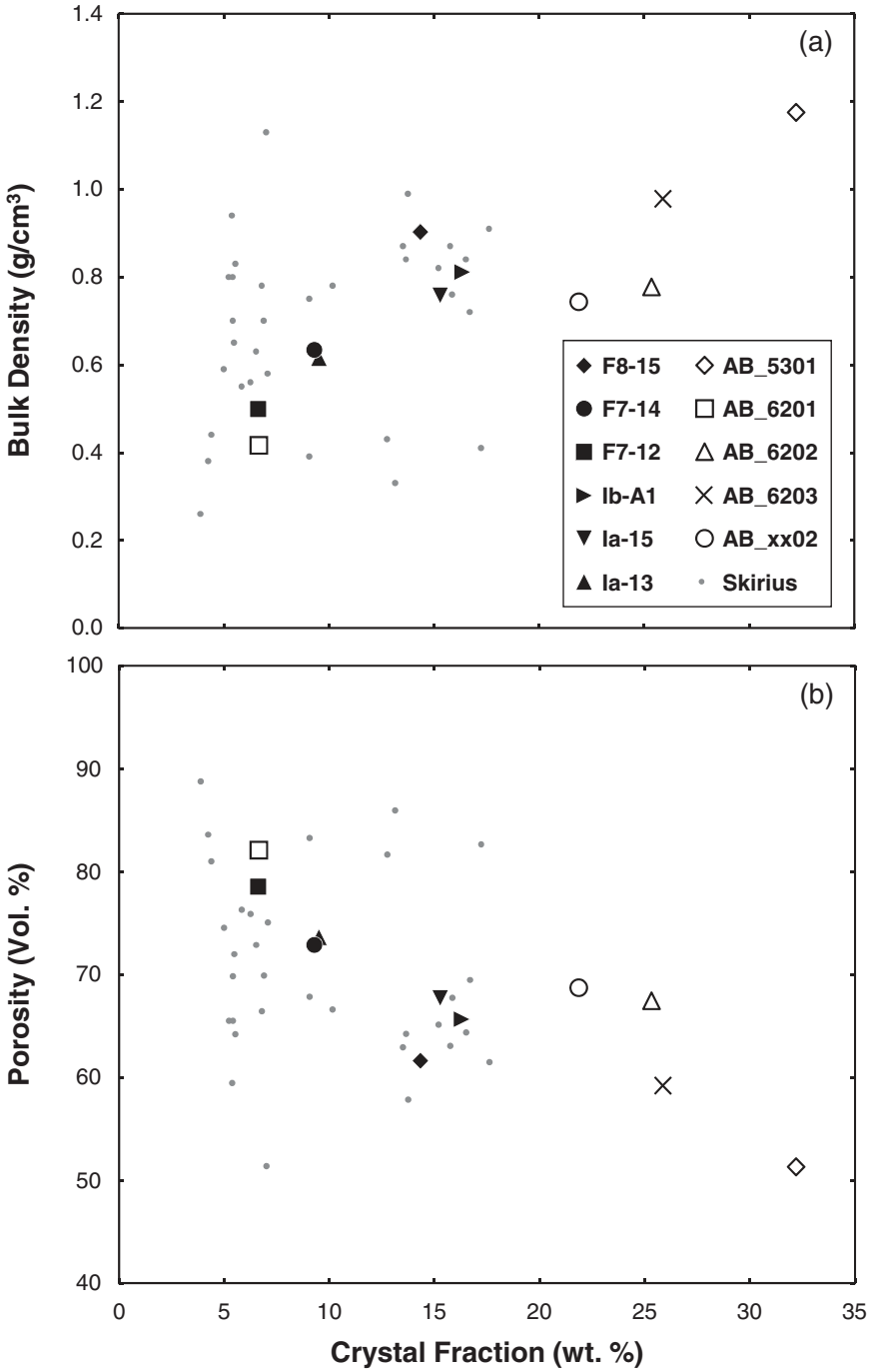

Fig. 5. Plots of crystallinity (crystal mass fraction) vs pumice clast bulk density and porosity (pore volume fraction) in early- and late-erupted pumice clasts. It should be noted that crystallinity and porosity are inversely correlated, resulting in a positive correlation between density and crystallinity. Four of our five late-erupted pumice clasts have the highest crystallinities of the whole dataset (25–32 wt. % crystals), along with relatively high density (0·74–1·18 g cm^{-3}) and low porosity (51–69%). The fifth pumice clast (AB.6201) has the lowest density (0·42 g cm^{-3}) and crystallinity (6·6 wt. %) and highest porosity (82%) among those studied here and by Gualda *et al.* (2004). Small dots labeled 'Skirius' are from Skirius *et al.* (1990).

>70 μm; and the interval 35–70 μm is characterized by a drop in population density of nearly an order of magnitude from the population densities in adjacent bins (Figs 8b and 9a).

It is interesting to note that these crystal size distributions are similar in shape to the whole-crystal quartz size distributions (obtained by crushing and sieving) for intermediate-density early-erupted pumice clasts (samples

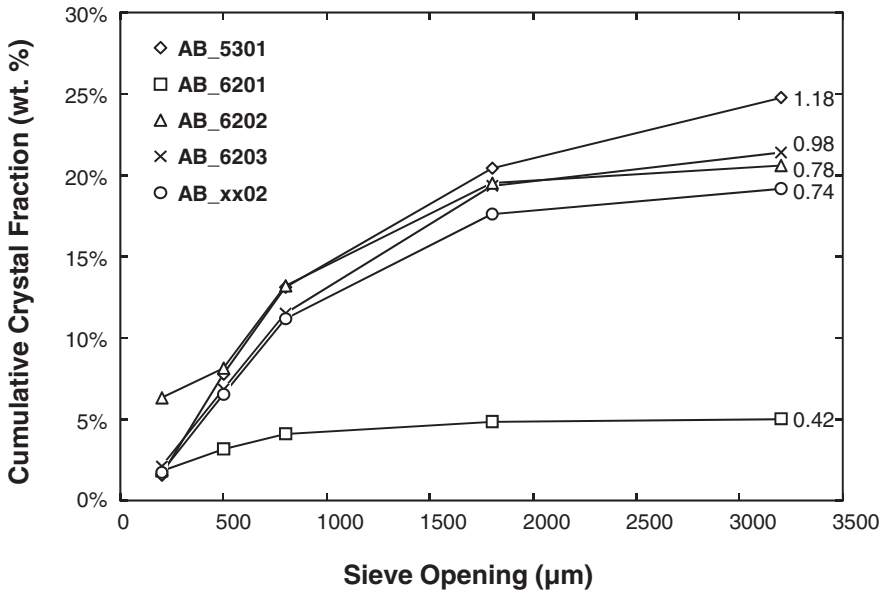

Fig. 6. Plot of sieve size vs cumulative crystal fraction for late-erupted pumice clasts. Values close to each curve correspond to bulk clast density (in g cm^{-3}). Noteworthy features are the similarity in mass fractions of crystals <250 μm (except for AB.6202) and the sharp increase in mass fraction with size (except AB.6201), demonstrating that crystallinity is strongly correlated with the presence of large crystals (see also Fig. 7).

F7-14 and Ia-13; Fig. 9a) studied by Gualda *et al.* (2004), in particular what we call here Part (2) of the distributions. Unfortunately, the extensive fragmentation of quartz crystals in the early-erupted pumice has made it impractical to quantify the abundances of crystals <50 μm in the early-erupted pumice, as this size range is dominated by crystal fragments. It is thus unknown if Part (1) of the size distributions observed here is present in the early-erupted pumice.

High-density clast. The quartz + feldspar size distribution of the high-density clast, AB.5301 (1·18 g cm^{-3}), has a similar general shape to the intermediate-density clast distributions, but it is shifted towards larger sizes (Fig. 9b), such that the boundaries between the three sections of the size distributions are shifted accordingly: Part (1) includes crystals <70 μm, Part (2) shows a shallow distribution for crystals >140 μm, and Part (3) reveals a modest drop in the abundance of crystals sized between 70 and 140 μm. The shape of the crystal size distribution obtained for the high-density clast AB.5301 also compares favorably with that of the high-density early-erupted clasts (samples F8-15 and Ia-15; Fig. 9b) studied by Gualda *et al.* (2004).

Low-density clast. The quartz + feldspar size distribution of the low-density late-erupted pumice clast, AB.6201 (0·42 g cm^{-3}), is somewhat distinct (Fig. 9c): similar to the high-density clast distribution, Part (1) extends to crystal sizes <70 μm, Part (2) includes crystals >140 μm, and Part (3) includes the range of crystal sizes between 70 and 140 μm. Part (3) is significantly different from the other distributions. Even though the distribution does not follow the smooth concave-up curve of the magnetite and pyroxene + biotite distributions, the distinct drop seen in the other quartz + feldspar distributions is notably absent. Instead, between crystal sizes of 70 μm and 140 μm, there is a visible kink in the distribution; this kink is the manifestation of the more pronounced drops seen in the intermediate- and high-density clast quartz + feldspar distributions, as discussed below. Yet again, low-density clasts from the early- and late-erupted Bishop show crystal size distributions with similar shape.

DISCUSSION

Pumice density, crystallinity and porosity correlations

In combination, the early-erupted pumice clasts studied by Gualda *et al.* (2004) and the late-erupted clasts studied here span much of the spectrum of pumice bulk density, crystallinity and porosity reported for the quickly cooled Bishop Tuff pumice clasts studied by Skirius *et al.* (1990), Wallace *et al.* (1999), and Anderson *et al.* (2000).

The strong positive correlation between crystallinity and bulk density (Fig. 5a) strongly suggests that crystal abundance is a major control on pumice density (in combination with vesicle volume; see below). In particular, the cumulative mass fraction distributions (Fig. 6) indicate that large crystals play a particularly important role. It is not numbers so much as the size of crystals that is important; even though the largest crystals are not particularly abundant, they concentrate most of the crystal mass, and pumice clasts in which they appear have the highest crystallinities and densities, despite the higher total crystal

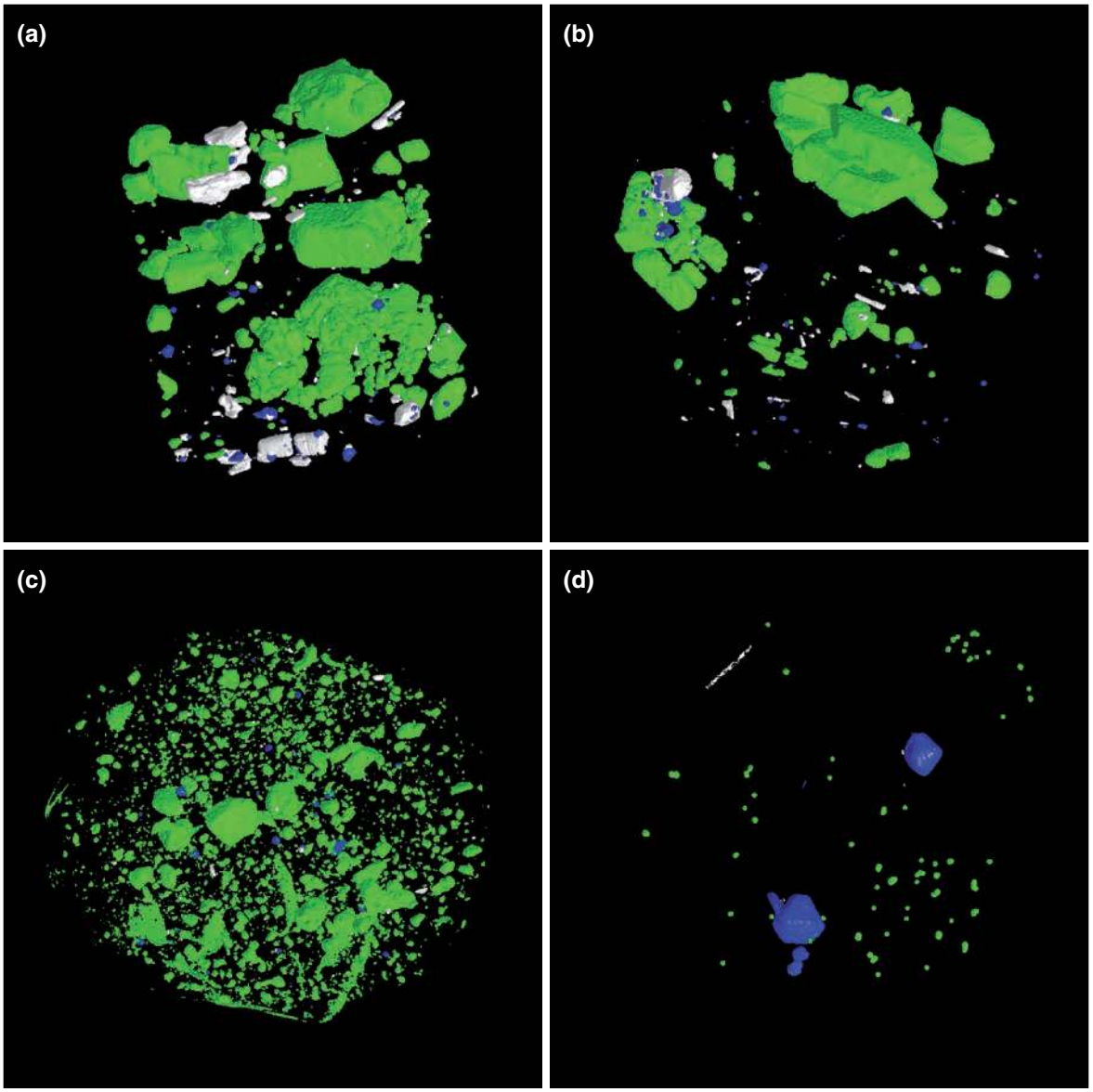

Fig. 7. (a–c) Three-dimensional images of A runs (17 μm per voxel) for pumice clasts: (a) AB.5301; (b) AB.6203; (c) AB.6201. Magnetite is dark gray (blue in the online version), biotite and pyroxene are white, quartz and feldspars are light gray (green online). Low-density pumice clast AB.6201 has many small crystals and no large crystals, whereas high-density pumice clast AB.5301 has a few very large crystals; intermediate-density pumice clast AB.6203 has more comparable abundances of small and large crystals. (d) Three-dimensional image of D run (2·5 μm per voxel) for pumice clast AB.6202. Abundant small (<50 μm) quartz and feldspar crystals (see text for discussion), and sparse euhedral magnetite crystals, should be noted. Animated versions can be seen in Movies 1–4 in the online Supplementary Data.

number densities in other clasts (resulting from the higher abundance of small crystals).

This idea is further supported by the variations in crystal populations qualitatively observed in 3D renditions of the samples (Fig. 7). In these volumes, the high-density clast (Fig. 7a) is seen to have a large number of very large crystals. Intermediate-density clasts (Fig. 7b) contain abundant large crystals, but smaller crystals are more numerous than in the high-density clast. The low-density clast (Fig. 7c) has a comparative enrichment of very small crystals and few to no large crystals. The control of the abundance of large crystals on bulk density and crystallinity becomes apparent on comparing these observations with Figs 5 and 6.

As observed by Gualda *et al.* (2004), porosity shows a striking negative correlation with crystallinity and bulk density, and the same correlation is observed in our late-erupted pumice clasts (Fig. 6b). As emphasized by

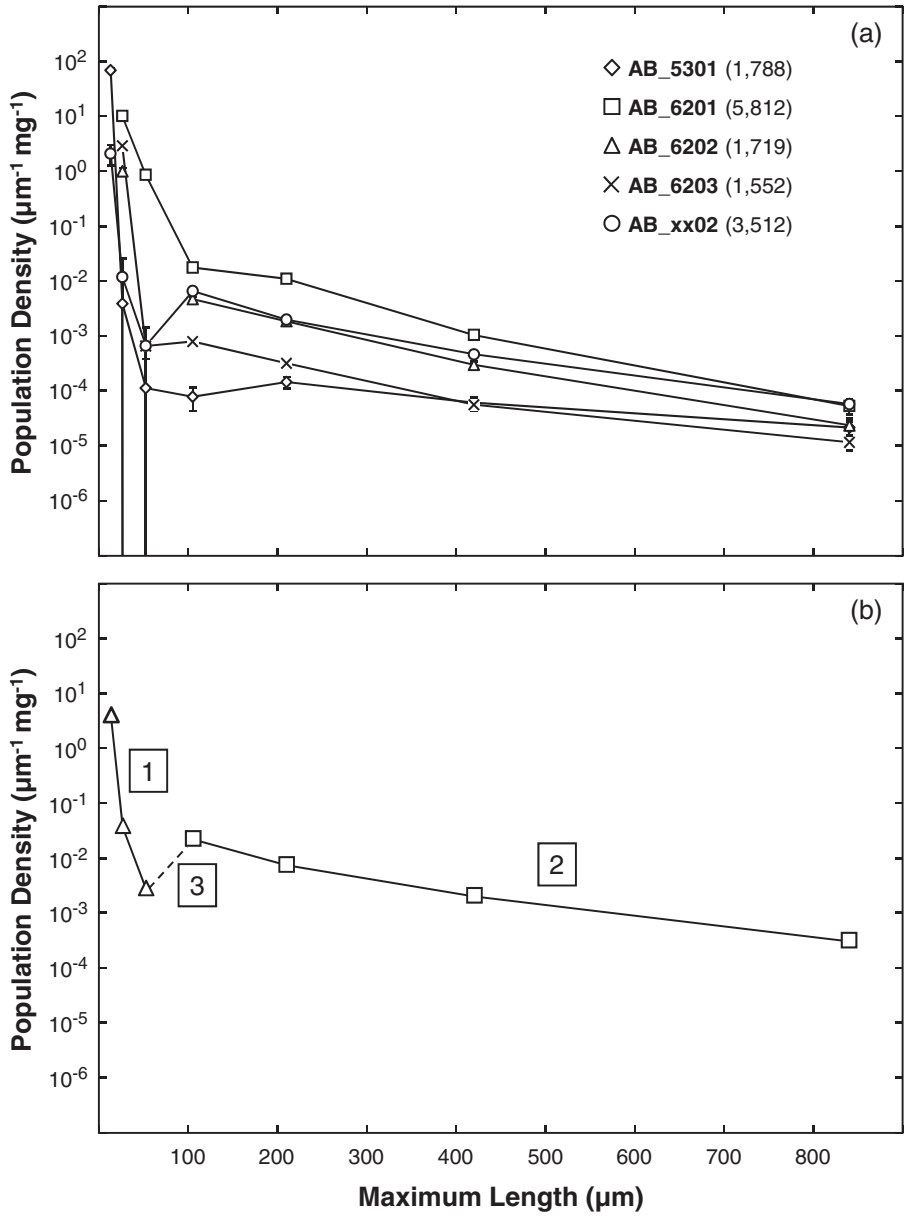

Fig. 8. (a) Quartz + feldspar crystal size distributions for the late-erupted pumice clasts. It should be noted that size distributions vary significantly from sample to sample. (b) Quartz + feldspar crystal size distributions for sample AB.xx02 showing the three regions present in the crystal size distributions of all five pumice clasts (see text for discussion). Error bars are due to counting statistics only and thus correspond to minimum estimates (Gualda, 2006); where absent, error bars are smaller than the symbol.

Gualda *et al.* (2004), this correlation is puzzling, given that gas-saturated magmas—as the Bishop magma is believed to have been (Wallace *et al.*, 1995, 1999; Anderson *et al.*, 2000; Gualda & Anderson, 2007)—would exsolve gas during crystallization. While the effect of simultaneous crystallization and bubble exsolution on magma density will depend on the density of the fluid phase under magmatic conditions, bubble expansion and growth during decompression will invariably lead to positive correlations between pumice porosity and crystallinity, which is opposite to what we observe for both early- and late-erupted pumice.

In light of the suggestion by Anderson *et al.* (2000) that quartz and sanidine crystals might have sunk hundreds of meters during their crystallization history, Gualda *et al.* (2004) interpreted the negative correlation between porosity and crystallinity as a result of relative migration of crystals and bubbles. Anderson *et al.* (2000) observed that sanidine crystals are reversely zoned, with Ba-poor cores and Ba-rich rims, which is inconsistent with closed-system

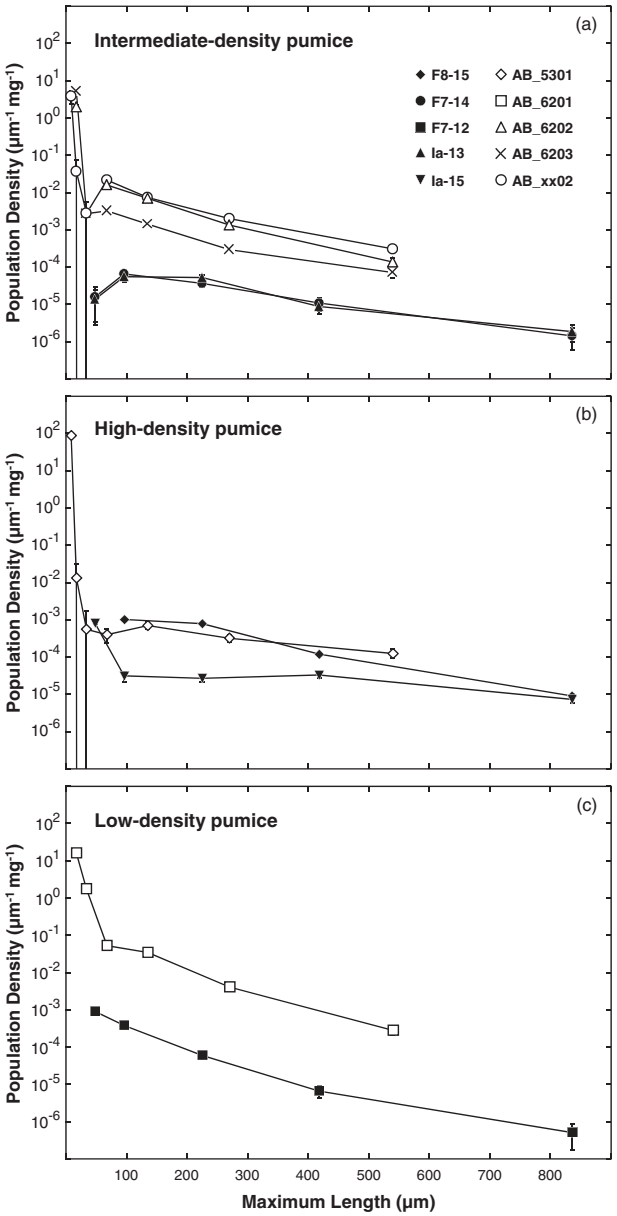

Fig. 9. Quartz + feldspar crystal size distributions for late-erupted pumice (open symbols) distinguished by density categories and compared with whole-quartz crystal size distributions for early-erupted pumice (closed symbols; data from Gualda *et al.*, 2004) of corresponding density category: (a) intermediate-density pumice; (b) high-density pumice: (c) low-density pumice. The similarities between early- and late-erupted crystal size distributions in each density category should be noted.

crystallization, given that they estimated that Ba should be compatible in the Bishop magma. They further observed that some quartz crystals with multiple melt inclusions show a rimward increase in CO_2, consistent with crystallization over increasing pressures (under the assumption of closed-system crystallization). They tried to reconcile these observations by suggesting that quartz and sanidine grew while they sank hundreds of meters (pressure change of ~0·5 kbar), causing them to sample progressively less differentiated melt. Although crystal sinking alone will result in a negative correlation between porosity and crystallinity, the resulting slope is much shallower than what we observe (see Gualda *et al.*, 2004), and that was the basis for Gualda *et al.* (2004) to suggest that crystal sinking would have to be accompanied by bubble rising to explain the observed porosity–crystallinity trends. The viability of this crystal sinking + bubble rising mechanism has to be questioned in view of recent work suggesting that (1) the crystal sinking mechanism advanced by Anderson *et al.* (2000) is an unlikely explanation for quartz and sanidine rims, given that new cathodoluminescence and trace-element data on quartz and sanidine reveal sharp boundaries between crystal rims and interior regions, inconsistent with gradual sinking (see Gualda, 2007; Gualda *et al.*, 2007, and unpublished data; Wark *et al.*, 2007); and (2) that the timescales of quartz crystallization—of the order of only a few thousand years (see Crowley *et al.* 2007; Gualda *et al.*, 2007, and unpublished data)—make it difficult for significant crystal sinking and bubble rising to occur and cause the development of the observed inverse relationship. We are thus unable to identify a mechanism capable of satisfactorily explaining both this inverse correlation and the gradients in CO_2 concentration in quartz-hosted melt inclusions documented by Anderson *et al.* (2000). Studies of vesicle size distributions and trace element zoning in quartz and sanidine currently under way are likely to provide additional information that will aid further scrutiny of the problem.

Magnetite, biotite, and pyroxene size distributions

Crystal size distributions developed under magmatic conditions are typically log–linear in shape, and the origin of such distributions is relatively well understood (e.g. Marsh, 1988*b*, 1998). Fractal size distributions, such as those seen for magnetite and pyroxene + biotite in the late-erupted pumice, have also been documented, but are typically considered to result from crystal fragmentation (Marsh, 1998; Bindeman, 2005; Gualda, 2006; Higgins, 2006). However, in tomographic images of both early- and late-erupted clasts (e.g. Fig. 7), magnetite, biotite and pyroxene are found to be whole crystals, often with distinct crystal faces visible. In this sense, the magnetite and pyroxene + biotite fractal size distributions obtained here are unexpected, and suggest that processes other than fragmentation are probably capable of generating fractal size distributions (for further discussion, see Pamukcu & Gualda, 2010).

Quartz and feldspar size distributions

Quartz and feldspar size distributions obtained here record important aspects of the crystallization history of

the Bishop magma. We start by discussing the potential origin of the contrast in crystal fragmentation history between our early- and late-erupted pumice clasts; we then explore the shapes of the quartz + feldspar size distributions and discuss their significance for the various stages of crystallization of the Bishop magma; we conclude with inferences about the timescales for these crystallization stages.

Crystal fragmentation

One of the challenges in studying the textures of the early-erupted Bishop pumice is the fact that quartz and feldspar crystal fragmentation is widespread. In early-erupted samples, data from both crystal separates and tomography yield fractal size distributions characteristic of fragmentation processes, and quartz and feldspar crystals appear broken or as fragments in the tomography images. Thus, Gualda *et al.* (2004) determined crystal size distributions for whole, glass-coated quartz crystals to assess crystal size distributions representative of the pre-fragmentation state in the early-erupted pumice (glass-coated feldspar crystals are much rarer, seemingly a result of the lower abundance of feldspar and the potentially higher probability of breakage of feldspar crystals; Gualda *et al*, 2004). As a result, the whole-quartz size distributions are biased towards low population densities, as a considerable proportion of glass-coated crystals initially present is likely to have broken during processing. These distributions may also be biased owing to preferential breakage of larger crystals; however, this is probably a relatively minor effect, at least in the range of crystal sizes studied by Gualda *et al.* (2004; i.e.~35–1000 μm). It is noteworthy that a small proportion of quartz fragments are entirely glass-coated, suggesting that fragmentation was at least partly a magmatic (i.e. pre-eruptive or early syn-eruptive) process.

In light of these observations, the favorable comparison between the shapes of the early-erupted whole-quartz size distributions (determined by crushing–sieving–winnowing) and the shape of late-erupted quartz + feldspar size distributions (obtained using X-ray tomography) is significant. Importantly, this reveals that quartz and feldspar in our late-erupted pumice clasts were not subject to the same fragmentation processes that affected the early-erupted pumice clasts. This is corroborated by the crystal shapes observed in the late-erupted pumice clasts (Fig. 7), which are typically euhedral, often preserving Carlsbad twins in sanidine (see Fig. 7b). The agreement also suggests that the approach of using whole, glass-coated crystal size distributions as a proxy for pre-fragmentation quartz size distributions is reasonable. We note that whereas the early-erupted pumice studied by Gualda & Rivers (2006) are all from ash-fall units, the late-erupted pumice studied here are all from ash-flow units; hence, it is unclear whether the contrast in fragmentation behavior is due to different histories for early- vs late-erupted pumice, or from differences in eruptive history between ash-fall and ash-flow deposits. Study of pumice clasts from ash-flow unit IglEb of the early-erupted Bishop should shed light into this matter. A few large quartz and sanidine crystals are broken into some tens to hundreds of fragments, with coarsely vesicular glass (up to 500 μm diameter vesicles) in the space separating the fragments (Fig. 10). In some of them where fragmentation is limited, the glass emanates from a particular region in the crystal. These features suggest that in these cases fragmentation is due to melt inclusion decrepitation (Tait, 1992). In most cases, these fragments (at least the larger ones) were merged during image processing, resulting in a single large crystal of complex shape but approximately correct volume (for a discussion, see Gualda & Rivers, 2006). As such, we minimized the potential influence of this fragmentation process in the quartz + feldspar size distributions discussed below.

Crystallization stages

As indicated above, quartz + feldspar size distributions can be broadly divided into three parts (Fig. 8b), one characteristic of small crystals (35–70 μm), one including larger crystals (70–140 μm), and one corresponding to the transition between these two regions. Quartz + feldspar size distributions of the three intermediate-density clasts are very similar to each other, but those of the high- and low-density clasts differ noticeably (Fig. 9). These three parts of the size distributions reveal the nucleation and growth dynamics in the Bishop magma body.

The shallow slope of Part (2) and the relatively large size of its crystals are indicative of prolonged growth (see below); the log–linear shape can be interpreted as resulting from a single growth stage or regime (e.g. Marsh, 1988*b*, 1998). Gualda *et al.* (2004) interpreted this to correspond to slow growth under pre-eruptive conditions, over relatively extended periods of time. Our new results are in agreement with this interpretation. The drop in number density characteristic of Part (3) is also observed in the early-erupted pumice, and recognition of it was critical to the interpretation of the whole-quartz size distributions (Gualda *et al.*, 2004). The relative paucity of crystals of ~50–100 μm size reveals that nucleation rates were low during growth of the larger crystals that constitute Part (2) of the distribution; thus, the total number density of crystals remained relatively low, and small crystals gradually grew out of existence (i.e. by becoming larger), giving rise to the drop in number density observed in the crystal size distributions. We interpret this to represent a period of pre-eruptive crystallization dominated by crystal growth with limited nucleation. These characteristics—and their similarity to what we observed in the early-erupted pumice—are compatible with the interpretation of Gualda *et al.* (2004) that crystal size distributions record crystal growth in a large magma body crystallizing

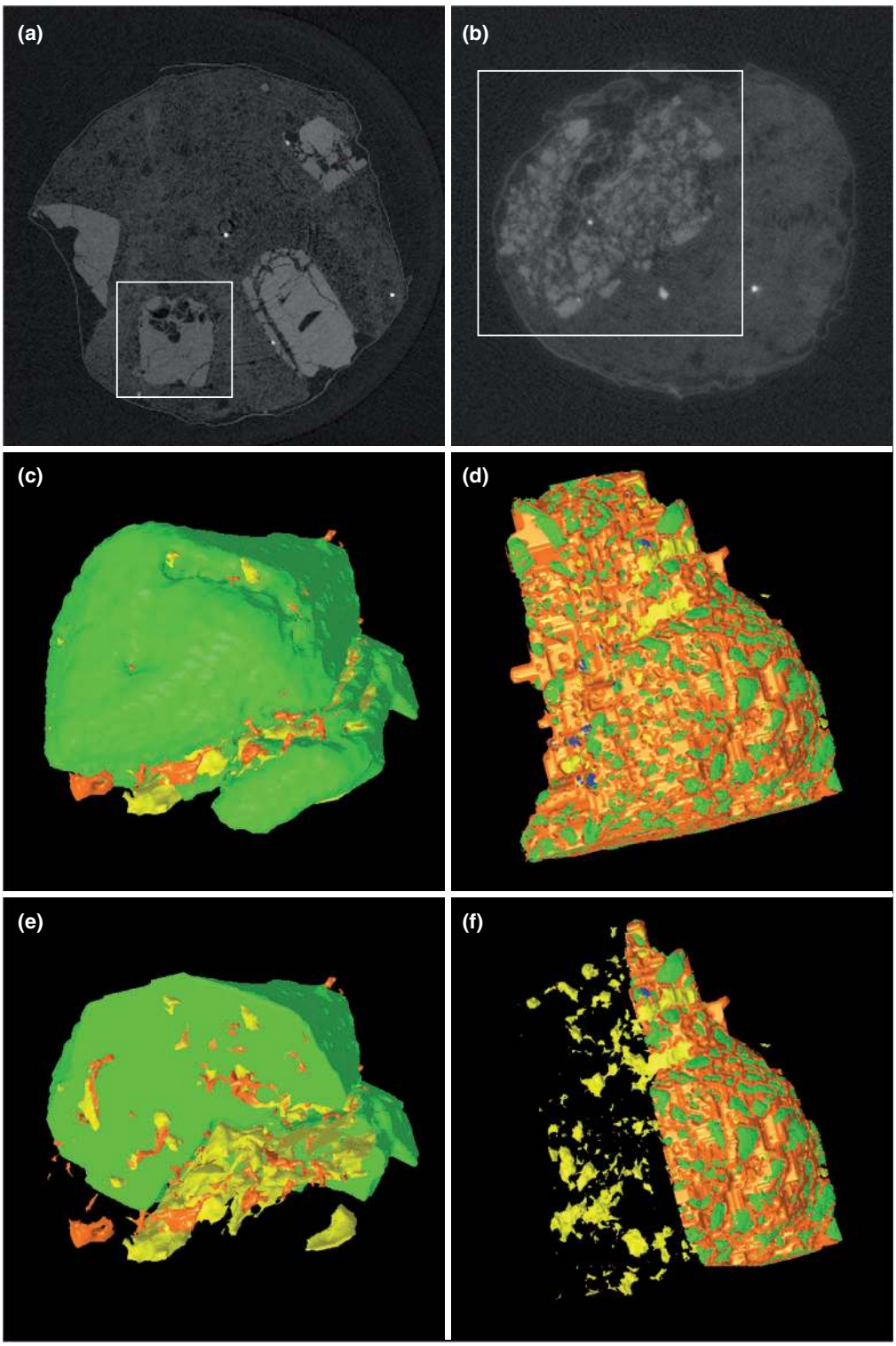

Fig. 10. Tomographic images showing fragmented crystals with vesiculated melt along fractures, suggesting formation by melt inclusion decrepitation. (a, b) Slices through tomograms of sample AB.6203; resolution is 17 μm per voxel, and field of view is ~11 mm wide. (c–f) Three-dimensional reconstructions of the crystals in (a) and (b); field of view is *c.* 3 mm in (c) and (e), and 6·5 mm in (d) and (f); medium gray (green in the online version) indicates feldspar; white (yellow online), large spaces occupied by air, mostly large vesicles; dark gray (orange online), finely vesiculated glass; sparse black (blue online), magnetite. Parts of the crystals and glass were omitted in (e) and (f) to better show the distribution of large vesicles. The presence of large vesicles and thin films in the denoted crystal in (a) should be noted; glass emanates from a bulge in the center of the crystal, as seen in (e). Fracturing is much more extensive in the crystal in (b), with vesiculated glass pervasively occupying the spaces between the numerous fragments. Animated versions of (c)–(f) are shown in Movies 5–8 in the online Supplementary Data.

under small degrees of undercooling, which would dampen nucleation and favor crystal growth.

Part (1), in turn, shows high population densities concentrated in the very small bin sizes, with characteristic population densities in excess of two orders of magnitude larger than the maximum values observed for Part (2). It is unlikely that these small crystals grew after deposition: these pumice clasts were deposited within 1–2 m of the underlying granite and cooled rapidly, which minimized growth after deposition. Whereas some melt inclusions in these clasts are partly devitrified and have crystals up to a few micrometers long (Anderson *et al.*, 2000, fig. 3; Wallace *et al.*, 2003, fig. 3), cracked, degassed melt inclusions (Wallace *et al.*, 2003, fig. 3i) have large bubbles and are crystal-free. This suggests that H_2O loss inhibited crystal nucleation and growth, and only undegassed melt inclusions devitrified. Given that the vesicular glass of these pumice clasts degassed during decompression and eruption, the evidence from melt inclusions suggests that post-deposition devitrification was suppressed, and we conclude that the small crystals that constitute Part (1) formed before or during eruption.

We interpret these crystals to have developed during a period of significant nucleation, and they did not have enough time before eruption to grow to sizes larger than *c.* 50 μm. Thus, we infer that a significant change in the conditions in the magma body took place and gave rise to a distinct nucleation event shortly before eruption. Steep crystal size distributions for small sizes are commonly observed in volcanic rocks (e.g. Cashman, 1988), and correspond to the groundmass grown under syn-eruptive conditions. Our observations are entirely compatible with such an interpretation. As such, the small quartz and feldspar crystals observed in our highest resolution datasets (Fig. 7d) correspond to the groundmass of the Bishop pumice, inferred to have grown syn-eruptively; that the groundmass is poorly developed is in agreement with the very high eruption rates calculated for eruptions of the magnitude of the Bishop Tuff (Carey & Sigurdsson, 1989; Wilson & Hildreth, 1997; Dufek & Bergantz, 2007), leaving little opportunity for groundmass crystallization.

In summary, Part (2) of the quartz + feldspar size distributions corresponds to the pre-eruptive stages of growth; limited nucleation during growth of Part (2) leads to the development of the drop characteristic of Part (3). Part (1), on the other hand, corresponds to syn-eruptive growth of the Bishop groundmass. Complexities and departures from the more typical pattern observed for the intermediate-density pumice clasts can be explained by differences in the shape of the pre-eruptive crystal size distribution. This is shown in Fig. 11, where the same population of small crystals is added to pre-existing populations of larger crystals; it should be noted that the resulting size distributions are qualitatively similar to those observed. The variations in the pre-eruptive population would presumably map different portions of the magma body; for instance, it is likely that more marginal regions of the magma body would experience higher nucleation rates than more central portions, but specific matching of pumice clasts to particular regions in the magma body at this point would be excessively speculative.

Although the variations in the pre-eruptive populations indicate that the pre-eruptive histories of different parcels in the magma body were potentially distinct, the presence of a similar population of small crystals in all five of the late-erupted pumice clasts studied here indicates that just prior to eruption a major event took place that had a widespread and consistent effect over much of the magma body, if not the whole of it. A nucleation event as inferred here requires a sudden increase in the degree of supersaturation of the system. Cooling of such a large body as the Bishop Tuff is unlikely to be a plausible mechanism, as the sudden development of steep thermal gradients would be limited by the low thermal conductivity of silicic rocks and magmas, with the result that high degrees of supersaturation would be unlikely to develop. A sudden decrease in pressure in a water-saturated magma such as that of the Bishop Tuff (Wallace *et al.*, 1995; Gualda & Anderson, 2007), however, would be a reasonable explanation as it could lead to a high degree of supersaturation that would be transferred to the whole body rapidly, causing widespread nucleation in addition to crystal growth. If eruption occurred soon thereafter, crystals would have little time to grow and a significant population of small crystals would remain. The large number densities of tiny crystals expected to result from this process are precisely what are found in the quartz + feldspar distributions for the late-erupted pumice clasts.

Timescales of crystallization

Crystal size distributions can be used to constrain the timescales of crystal growth in magmatic systems (see Cashman & Marsh, 1988; Marsh, 1988*a*, 1998; Zieg & Marsh, 2002; among many others). Information comes from two properties of crystal size distributions, as follows.

(1) The maximum crystallization time of the system is given by the growth time of the largest crystal, which can be calculated by $t_{max} = G/L_{max}$, where G is growth rate, t is time and L is crystal size (in linear dimension).

(2) The growth time of a population of crystals is related to the slope of the crystal size distribution on a log–linear plot of population density vs crystal size: $\text{slope} = -1/(Gt)$.

In both cases, the growth rates are assumed to be linear and independent of crystal size or time, in agreement with the theory of crystal size distributions developed by

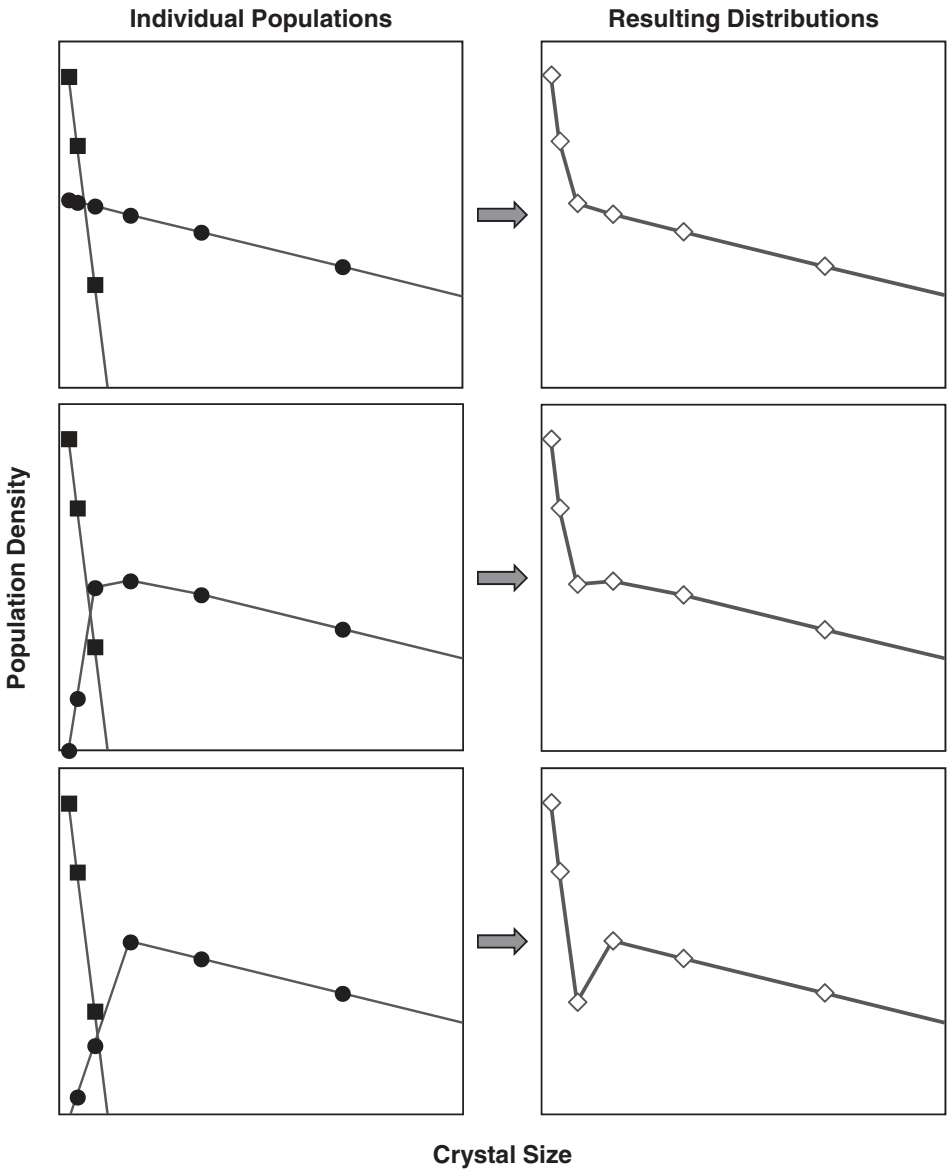

Fig. 11. Diagrams showing the effect on the resulting crystal size distributions of adding two populations of crystals. The resulting distribution for a pumice clast will be different depending on the shape of the distribution for each crystal population (see text for discussion). The similarity between size distributions obtained in this figure and those observed in Fig. 9 should be noted; the population of small crystals is the same in all three examples.

Marsh (1988*b*, 1998); importantly, no obvious violations to this assumption have been reported to date (see Zieg & Marsh, 2002).

It should be noted that, to derive timescale estimates, it is necessary to know the growth rate of the mineral in question. Mineral growth rates have been estimated from a variety of textural features, including from crystal size distributions where growth times can be independently constrained (e.g. Cashman, 1992) and from compositional zoning patterns (e.g. McCanta *et al.*, 2007). Anderson *et al.* (2000) presented a variety of estimates for quartz growth rates, and they constrained phenocryst growth rates to be $4 \times 10^{-13}\,\mathrm{m\,s^{-1}}$. Recently, Gualda *et al.* (2007, and unpublished data) used Ti zoning patterns in quartz from early-erupted Bishop pumice to constrain quartz growth rates at $>10^{-13}\,\mathrm{m\,s^{-1}}$ for crystal rims, and at $\sim10^{-14}\,\mathrm{m\,s^{-1}}$ for crystal interiors. Interestingly, not only are these growth rates within the constraints placed by the analysis of Anderson *et al.* (2000), but they are also in remarkable agreement with growth rates calculated for plagioclase in dacites, where rim and groundmass growth rates are estimated to be in the range 10^{-9}–$10^{-13}\,\mathrm{m\,s^{-1}}$ (see McCanta

et al., 2007, and references therein), whereas phenocryst growth rates are estimated to be in the range 10^{-13}–10^{-14} m s^{-1} (Cashman, 1988). The contrast between groundmass and phenocryst growth rates is often attributed to a difference between cooling-induced crystallization under low degrees of supersaturation and decompression-induced crystallization under high degrees of supersaturation (e.g. Cashman, 1992). Based on our conclusion that the shallower portion of the quartz + feldspar size distributions [Part (2)] corresponds to pre-eruptive growth under low degrees of supersaturation (see above), we use a conservative growth rate of 10^{-14} m s^{-1} for the larger crystals. For the steeper portion of the distribution [Part (1)] grown syn-eruptively under higher degrees of supersaturation, we use a conservative minimum growth rate of 10^{-13} m s^{-1}, bearing in mind that growth rates may have been a few orders of magnitude faster.

Determining the maximum crystal size in a deposit of >600 km^3 is a challenging, if not impossible, task. We point out, however, that crystals in excess of 2–3 mm are very rare in the Bishop pumice, and we have never observed any crystals as large as 1 cm. Based on our crystal size distributions, we estimate that >95% of the quartz + feldspar crystal mass is included in crystals <2 mm, and >99% of the quartz + feldspar crystal mass is included in crystals <3 mm. As such, an appropriate maximum growth time for quartz + feldspar crystals is of the order of ~5000 years ($1{\cdot}5 \times 10^{11}$ s).

Growth times based on the slopes of the size distributions were also obtained (Fig. 12, Table 2). Slopes for the large crystal population of early- and late-erupted quartz + feldspar crystals are similar to each other and yield $Gt = 137$–788 μm, corresponding to ~400–2500 years of growth time for 10^{-14} m s^{-1} growth rates. The best value for the pooled late-erupted data corresponds to a growth time of 600 years, and 900 years are obtained for the early-erupted data (Table 2). For the late-erupted small crystal population, $Gt = 3{\cdot}5$–$7{\cdot}0$ μm, corresponding to growth times of 1–2 years for growth rates of 10^{-13} m s^{-1}. The pooled late-erupted small crystal population data yield $Gt = 4{\cdot}9$ μm and $t = 1{\cdot}5$ years.

The agreement between estimates based on maximum crystal size and the slope of the large crystal populations is encouraging, and suggests a relatively short crystallization history for quartz and feldspars in the Bishop magma, on millennial timescales. This timescale is 1–2 orders of magnitude shorter than that inferred from zircon geochronology based on ion microprobe data (Simon & Reid, 2005), and is in good agreement with the timescales inferred from bulk zircon thermal ionization mass spectrometry measurements (Crowley *et al.*, 2007). Because crystal volumes are dominated by rim volumes (owing to the radius cubed effect), we interpret the agreement between quartz and feldspar growth times and bulk zircon geochronology timescales to mean that most of the zircon mass crystallized simultaneously with quartz and feldspar. This is likely to correspond to the crystallization time of the Bishop magma. The timescales recorded by zircon crystal cores reflect a different process, probably related to the construction (rather than crystallization) of a giant magma body as the Bishop system is thought to have been (for more details, see Gualda *et al.*, 2007, and unpublished data).

CONCLUSIONS

In this paper, we present qualitative textural data and crystal size distributions for late-erupted Bishop pumice obtained using a combination of X-ray tomography and bulk pumice determinations. We compare our results with similar data obtained by Gualda *et al.* (2004) and Gualda & Rivers (2006) for early-erupted Bishop pumice.

Late-erupted pumice clasts show a striking positive correlation between crystallinity and bulk density and an inverse correlation between porosity and crystallinity. The new data extend the trend observed by Gualda *et al.* (2004) towards significantly higher values of crystallinity and density, and lower porosity values. Although crystal sinking combined with bubble rising can explain the observed trend, recent work on quartz and sanidine trace-element zoning (Gualda, 2007; Wark *et al.*, 2007) and on the timescales of quartz and feldspar crystallization calls into question the viability of crystal sinking + bubble rising as an explanation for the observed inverse correlation between crystallinity and porosity.

Magnetite and pyroxene + biotite crystal size distributions for the late-erupted pumice clasts are similar to each other and can be described by power-law, or fractal, distributions. Such distributions are typically interpreted to result from crystal fragmentation; however, magnetite, pyroxene and biotite are observed to be euhedral in the 3D reconstructions, making fragmentation an unlikely explanation.

Quartz + feldspar crystal size distributions provide important information on the crystallization and crystal fragmentation history of the Bishop magma body, as follows.

(1) The widespread crystal fragmentation observed in early-erupted pumice is not evident in late-erupted pumice, as evidenced by the euhedral shapes of quartz and sanidine crystals in 3D reconstructions of late-erupted pumice, and the agreement between quartz + feldspar size distributions for late-erupted pumice and the whole, glass-coated crystal size distribution for early-erupted pumice of Gualda *et al.* (2004). Whether this distinction is due to different eruptive histories (i.e. early- vs late-erupted) or due

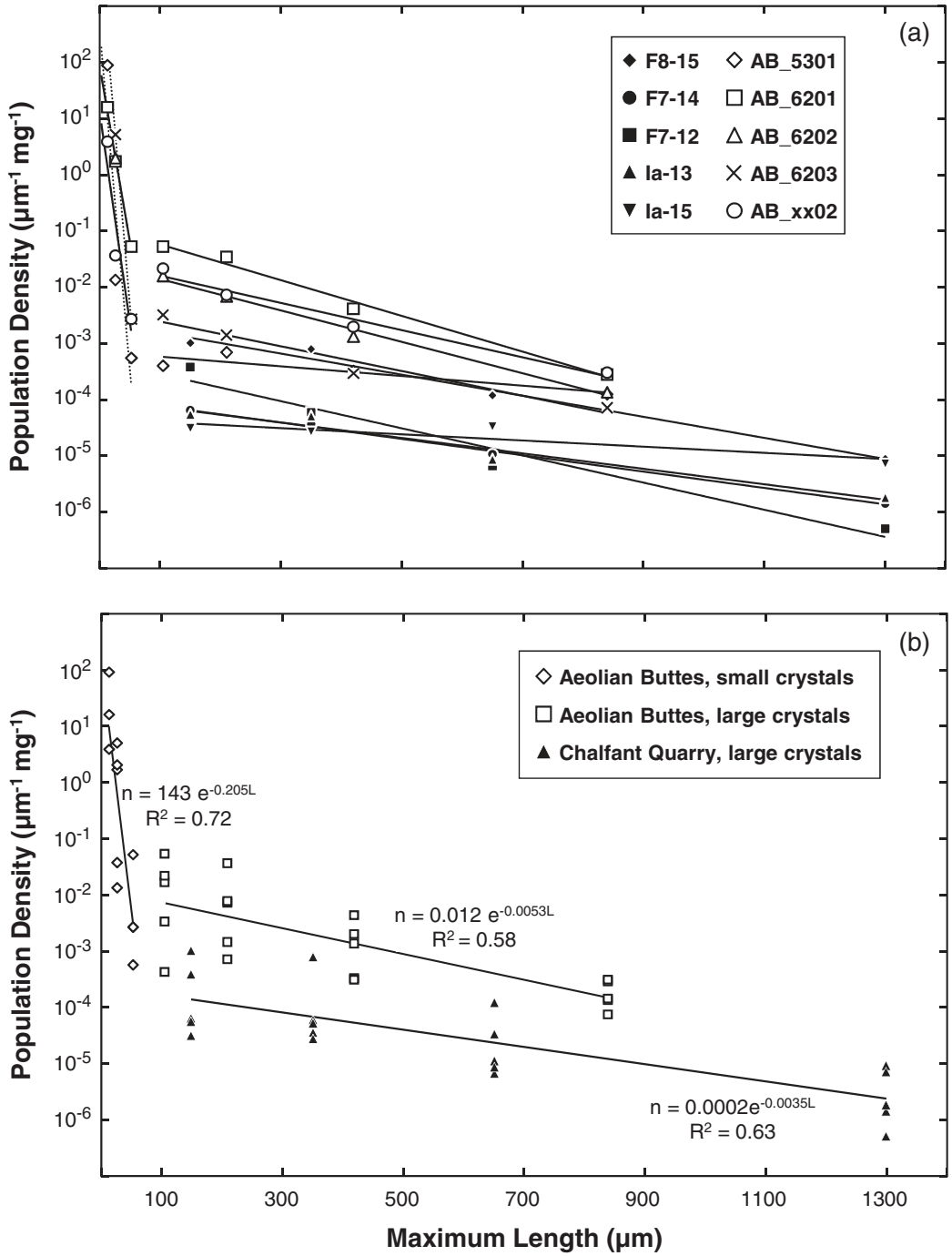

Fig. 12. (a) Best-fit exponential curves for populations of large (>100 μm) and small (<100 μm) quartz + feldspar crystals in late- and early-erupted pumice (see Table 2). (b) Best-fit exponential curves to aggregate quartz + feldspar crystal size distributions of small crystals in late-erupted pumice and for large crystals in early- and late-erupted pumice. The good quality of the fit suggests that the various samples had similar histories, particularly with regard to crystal growth times.

to the distinct mode of eruption (ash-fall vs ash-flow) is uncertain.

(2) Quartz and sanidine crystals in late-erupted pumice preserve evidence of melt inclusion decrepitation, as shown by fragmented single crystals with coarsely vesiculated glass filling up fractures and emanating from a center within the crystals.

(3) Crystal size distributions reveal the existence of two crystal populations: one including crystals larger than ~50 μm, which form a log–linear size

Table 2: Statistical parameters for best-fit exponential curves and estimated crystallization times for quartz + feldspar crystal size distributions of pumice clasts from early- and late-erupted Bishop Tuff

	Aeolian Buttes, large crystals					
	AB__5301	AB__6201	AB__6203	AB__6202	AB__xx02	All
$-1/Gt$	−0·0020	−0·0073	−0·0051	−0·0064	−0·0056	−0·0053
$\ln(n_0)$	0·001	0·12	0·004	0·027	0·028	0·012
r^2	0·80	0·99	0·96	0·99	0·97	0·58
df	2	2	2	2	2	18
F	8·2	180·9	42·6	204·2	77·6	25·3
p[a]	0·10	<0·01*	0·02*	<0·01*	0·01*	<0·01*
t[b]	1446	1823	1279	2206	1571	947
p[c]	<0·01*	<0·01*	<0·01*	<0·01*	<0·01*	<0·01*
Gt (μm)	505	137	197	155	179	189
t (a)[d]	1600	433	624	492	568	600
	Aeolian Buttes, small crystals					
	AB__5301	AB__6201	AB__6203	AB__6202	AB__xx02	All
$-1/Gt$	−0·28	−0·14	−0·29	—	−0·17	−0·20
$\ln(n_0)$	439·6	92·0	9898·3	—	14·1	143·2
r^2	0·81	1·00	1·00	—	0·88	0·72
df	1	1	0	—	1	10
F	4·2	261·7	—	—	7·3	26·0
p	0·29	0·04*	—	—	0·22	<0·01*
t	5·57	97·6	—	—	13·3	20·3
p	0·11	<0·01*	—	—	0·05*	<0·01*
Gt (μm)	3·6	7·0	3·5	—	5·8	4·9
t (a)	1·1	2·2	1·1	—	1·8	1·5
	Chalfant Quarry, large crystals					
	F712	F714	F815	Ia13	Ia15	All
$-1/Gt$	−0·0056	−0·0034	−0·0043	−0·0032	−0·0013	−0·0035
$\ln(n_0)$	0·000	0·000	0·002	0·000	0·000	0·000
r^2	0·96	1·00	0·98	0·95	0·79	0·63
df	2	2	2	2	2	18
F	48·6	740·3	117·0	39·4	7·3	30·7
p	0·02*	<0·01*	<0·01*	0·02*	0·11	<0·01*
t	1246	8084	2493	1978	2130	1562
p	<0·01*	<0·01*	<0·01*	<0·01*	<0·01*	<0·01*
Gt (μm)	180	298	232	316	788	283
t (a)	570	945	734	1002	2498	897

r^2, coefficient of determination (a value of unity indicates perfect correlation); df, degrees of freedom; F, F statistic.
[a]p, probability of Type-I error based on F statistic.
[b]t, Student t-statistic.
[c]p, probability of Type-I error based on Student t-statistic.
[d]t, growth time. Growth rates used: 10^{-14} ms^{-1} for large crystals; 10^{-13} ms^{-1} for small crystals (see text).
*Statistically significant at better than 95% confidence level.

distribution with relatively shallow slope, and another including smaller crystals, with much steeper log–linear size distributions. We interpret the larger crystal population to represent the pre-eruptive growth of quartz and feldspar crystals under relatively low degrees of supersaturation, as a result of slow cooling of a large body of crystal-poor magma. The smaller crystal population, in contrast, is interpreted to represent syn-eruptive nucleation and growth under significantly higher degrees of supersaturation, probably connected to eruptive decompression of the Bishop system.

(4) Using quartz growth rates derived by Gualda *et al.* (2007, and unpublished data) we estimate the timescales of growth for both the pre-eruptive and syn-eruptive crystal populations. We estimate that the pre-eruptive crystal population grew on millennial timescales, in agreement with recent geochronological determinations (Crowley *et al.*, 2007). We interpret this as being the timescale of crystallization of the Bishop magma body, whereas longer timescales recorded by zircon crystal cores probably reflect the construction of the crystal-poor Bishop magma body. Timescales for crystallization of the syn-eruptive crystal population are constrained at <1–2 years (possibly a few orders of magnitude shorter), and mark an important transition in the evolution of the Bishop magma body, probably the onset of eruptive decompression. These timescales have important implications for our understanding of giant magma bodies such as the Bishop system (Gualda *et al.*, 2007, and unpublished data).

ACKNOWLEDGEMENTS

We owe many thanks to Mark Rivers for the significant help he provided throughout this work. Portions of this work were performed at GeoSoilEnviroCARS (Sector 13), Advanced Photon Source (APS), Argonne National Laboratory.

FUNDING

GeoSoilEnvironCARS is supported by the National Science Foundation—Earth Sciences (EAR-0622171) and Department of Energy—Geosciences (DE-FG02-94ER14466). Use of the Advanced Photon Source was supported by the US Department of Energy, Office of Science, Office of Basic Energy Sciences, under Contract No. DE-AC02-06CH11357.

SUPPLEMENTARY DATA

Supplementary data for this paper are available at *Journal of Petrology* online.

REFERENCES

Anderson, A. T. (2010). Composite pumice in the Bishop Tuff. *Geological Society of America, Abstracts with Programs* **42**, 343.

Anderson, A. T., Davis, A. M. & Lu, F. Q. (2000). Evolution of Bishop Tuff rhyolitic magma based on melt and magnetite inclusions and zoned phenocrysts. *Journal of Petrology* **41**, 449–473.

Bailey, R. A., Dalrymple, G. B. & Lanphere, M. A. (1976). Volcanism, structure, and geochronology of Long Valley Caldera, Mono County, California. *Journal of Geophysical Research* **81**, 725–744.

Bindeman, I. N. (2003). Crystal sizes in evolving silicic magma chambers. *Geology* **31**, 367–370.

Bindeman, I. N. (2005). Fragmentation phenomena in populations of magmatic crystals. *American Mineralogist* **90**, 1801–1815.

Bindeman, I. N. & Valley, J. W. (2002). Oxygen isotope study of the Long Valley magma system, California: isotope thermometry and convection in large silicic magma bodies. *Contributions to Mineralogy and Petrology* **144**, 185–205.

Carey, S. & Sigurdsson, H. (1989). The intensity of plinian eruptions. *Bulletin of Volcanology* **51**, 28–40.

Cashman, K. V. (1988). Crystallization of Mount St. Helens 1980–1986 dacite—a quantitative textural approach. *Bulletin of Volcanology* **50**, 194–209.

Cashman, K. V. (1992). Groundmass crystallization of Mount St. Helens dacite, 1980–1986—a tool for interpreting shallow magmatic processes. *Contributions to Mineralogy and Petrology* **109**, 431–449.

Cashman, K. V. (1993). Relationship between plagioclase crystallization and cooling rate in basaltic melts. *Contributions to Mineralogy and Petrology* **113**, 126–142.

Cashman, K. V. & Marsh, B. D. (1988). Crystal size distribution (CSD) in rocks and the kinetics and dynamics of crystallization. 2. Makaopuhi Lava Lake. *Contributions to Mineralogy and Petrology* **99**, 292–305.

Crowley, J. L., Schoene, B. & Bowring, S. A. (2007). U–Pb dating of zircon in the Bishop Tuff at the millennial scale. *Geology* **35**, 1123–1126.

Dufek, J. & Bergantz, G. W. (2007). Dynamics and deposits generated by the Kos Plateau Tuff eruption: Controls of basal particle loss on pyroclastic flow transport. *Geochemistry, Geophysics, Geosystems* **8**, Q12O7.

Gualda, G. A. R. (2006). Crystal size distributions derived from 3D datasets: Sample size versus uncertainties. *Journal of Petrology* **47**, 1245–1254.

Gualda, G. A. R. (2007). Crystal and bubble populations in the early-erupted Bishop rhyolitic magma: microscopy, X-ray tomography and microanalysis of pumice clasts. PhD Thesis, University of Chicago.

Gualda, G. A. R. & Anderson, A. T. (2007). Magnetite scavenging and the buoyancy of bubbles in magmas. Part 1: Discovery of a pre-eruptive bubble in Bishop rhyolite. *Contributions to Mineralogy and Petrology* **153**, 733–742.

Gualda, G. A. R. & Rivers, M. (2006). Quantitative 3D petrography using X-ray tomography: Application to Bishop Tuff pumice clasts. *Journal of Volcanology and Geothermal Research* **154**, 48–62.

Gualda, G. A. R., Anderson, A. T. & Sutton, S. R. (2007). Rapid crystallization of the Bishop magma. *EOS Transactions, American Geophysical Union* **87(52)**, Fall Meeting Supplement, Abstract V24C-04.

Gualda, G. A. R., Pamukcu, A. S., Claiborne, L. L. & Rivers, M. L. (2010). Quantitative 3D petrography using X-ray tomography. 3. Documenting accessory phases with differential absorption tomography. *Geosphere* **6**, 782–792.

Gualda, G. A. R., Cook, D. L., Chopra, R., Qin, L. P., Anderson, A. T. & Rivers, M. (2004). Fragmentation, nucleation and migration of crystals and bubbles in the Bishop Tuff rhyolitic magma. *Transactions of the Royal Society of Edinburgh, Earth Sciences* **95**, 375–390.

Hervig, R. L. & Dunbar, N. W. (1992). Cause of chemical zoning in the Bishop (California) and Bandelier (New Mexico) magma chambers. *Earth and Planetary Science Letters* **111**, 97–108.

Higgins, M. D. (2006). Verification of ideal semi-logarithmic, lognormal or fractal crystal size distributions from 2D datasets. *Journal of Volcanology and Geothermal Research* **154**, 8–16.

Hildreth, W. (1977). The magma chamber of the Bishop Tuff: gradients in temperature, pressure, and composition. PhD Thesis, University of California Berkeley 328 p.

Hildreth, W. (1979). The Bishop Tuff: Evidence for the origin of compositional zonation in silicic magma chambers. In: Chapin, C. E. & Elson, W. E. (eds). *Ash-flow Tuffs. Geological Society of America, Special Papers* **180**, 43–75.

Hildreth, W. & Mahood, G. A. (1986). Ring-fracture eruption of the Bishop Tuff. *GSA Bulletin* **37**, 396–405.

Hildreth, W. & Wilson, C. J. N. (2007). Compositional zoning of the Bishop Tuff. *Journal of Petrology* **48**, 951–999.

Ketcham, R. A. (2005). Computational methods for quantitative analysis of three-dimensional features in geological specimens. *Geosphere* **1**, 32–41.

Ledbetter, M. T. & Sparks, R. S. J. (1979). Duration of large-magnitude explosive eruptions deduced from graded bedding in deep-sea ash layers. *Geology* **7**, 240–244.

Lowenstern, J. B., Smith, R. B. & Hill, D. P. (2006). Monitoring supervolcanoes: geophysical and geochemical signals at Yellowstone and other large caldera systems. *Philosophical Transactions of the Royal Society, Series A* **364**, 2055–2072.

Marsh, B. D. (1988*a*). Crystal capture, sorting, and retention in convecting magma. *Geological Society of America Bulletin* **100**, 1720–1737.

Marsh, B. D. (1988*b*). Crystal size distribution (CSD) in rocks and the kinetics and dynamics of crystallization. 1. Theory. *Contributions to Mineralogy and Petrology* **99**, 277–291.

Marsh, B. D. (1998). On the interpretation of crystal size distributions in magmatic systems. *Journal of Petrology* **39**, 553–599.

Marsh, B. D. (2007). Crystallization of silicate magmas deciphered using crystal size distributions. *Journal of the American Ceramic Society* **90**, 746–757.

McCanta, M. C., Rutherford, M. J. & Hammer, J. E. (2007). Pre-eruptive and syn-eruptive conditions in the Black Butte, California dacite: Insight into crystallization kinetics in a silicic magma system. *Journal of Volcanology and Geothermal Research* **160**, 263–284.

Pamukcu, A. S. & Gualda, G. A. R. (2010). Quantitative 3D petrography using X-ray tomography. 2. Combining information at various resolutions. *Geosphere* **6**, 775–781.

Rivers, M. L. & Gualda, G. A. R. (2009). 'tomo_display' and 'vol_tools': IDL VM packages for tomography data reconstruction, processing, and visualization. *EOS Transactions, American Geophysical Union* **90**, *Joint Assembly Supplement*, Abstract V13A-06.

Rivers, M. L., Sutton, S. R. & Eng, P. J. (1999). Geoscience application of X-ray computed microtomography. *Proceedings of SPIE. Developments in X-ray Tomography II* **3772**, 78–86.

Self, S. (2006). The effects and consequences of very large explosive volcanic eruptions. *Philosophical Transactions of the Royal Society, Series A* **364**, 2073–2097.

Simon, J. I. & Reid, M. R. (2005). The pace of rhyolite differentiation and storage in an 'archetypical' silicic magma system, Long Valley, California. *Earth and Planetary Science Letters* **235**, 123–140.

Skirius, C. M., Peterson, J. W. & Anderson, A. T. (1990). Homogenizing rhyolitic glass inclusions from the Bishop Tuff. *American Mineralogist* **75**, 1381–1398.

Smith, R. L. & Bailey, R. A. (1966). The Bandelier Tuff: A study of ash-flow eruption cycles from zoned magma chambers. *Bulletin of Volcanology* **29**, 83–103.

Tait, S. (1992). Selective preservation of melt inclusions in igneous phenocrysts. *American Mineralogist* **77**, 146–155.

Wallace, P. J., Anderson, A. T. & Davis, A. M. (1995). Quantification of pre-eruptive exsolved gas contents in silicic magmas. *Nature* **377**, 612–616.

Wallace, P. J., Anderson, A. T. & Davis, A. M. (1999). Gradients in H_2O, CO_2, and exsolved gas in a large-volume silicic magma system: Interpreting the record preserved in melt inclusions from the Bishop Tuff. *Journal of Geophysical Research—Solid Earth* **104**, 20097–20122.

Wallace, P. J., Dufek, J., Anderson, A. T. & Zhang, Y. X. (2003). Cooling rates of Plinian-fall and pyroclastic-flow deposits in the Bishop Tuff: inferences from water speciation in quartz-hosted glass inclusions. *Bulletin of Volcanology* **65**, 105–123.

Wark, D. A., Hildreth, W., Spear, F. S., Cherniak, D. J. & Watson, E. B. (2007). Pre-eruption recharge of the Bishop magma system. *Geology* **35**, 235–238.

Wilson, C. J. N. & Hildreth, W. (1997). The Bishop Tuff: New insights from eruptive stratigraphy. *Journal of Geology* **105**, 407–439.

Zieg, M. J. & Marsh, B. D. (2002). Crystal size distributions and scaling laws in the quantification of igneous textures. *Journal of Petrology* **43**, 85–101.